The International Journal of Advanced Manufacturing Technology (2018) 97:3655–3670
https://doi.org/10.1007/s00170-018-2210-8

ORIGINAL ARTICLE

An improved material constitutive model considering temperature-dependent dynamic recrystallization for numerical analysis of Ti-6Al-4V alloy machining

Yang Huang[1] · **Jingjing Ji**[1] · **Kok-Meng Lee**[1,2]

Received: 26 February 2018 / Accepted: 15 May 2018 / Published online: 29 May 2018

Abstract

Titanium alloys are well-known as hard-to-machine materials with a low thermal conductivity which gives rise to heat and thermal stress localization near the tool-chip interface during machining. The constitutive model that describes material behavior during severe deformation is fundamental to the fidelity of numerical simulations that offer a cost-effective method to study the machining process. However, the lack of understanding on the coupled temperature effects involved in the evolution of chip morphology, the constitutive model, which is essential for optimizing a machining process, is underexploited. This paper presents an improved Johnson-Cook material constitutive model (JCM-IM) to account the temperature-dependent factor, and its coupled effects between the critical strain and temperature on flow-softening of Ti-6Al-4V alloy during machining. Along with the procedure for implementing and calibrating the JCM-IM in a machining FEA software, the best-fit parametric values of the JCM-IM for characterizing orthogonal cutting of Ti-6Al-4V alloy are presented. The calibrated JCM-IM, which has been verified by comparing the simulated forces, chip morphology and overall/critical shear strains in the primary shear band over a wide range of cutting speeds and feed-rates, is capable of predicting different deformation mechanisms around the dynamic recrystallization onset temperature for machining of Ti-6Al-4V alloy. Several sets of simulation results, which agree well with experimental data, illustrate the effects of cutting speed on temperature distribution around friction/shear zones, chip morphology evolution, and shear strains in the primary shear zone. The numerical findings offer intuitive insights into the transition from a continuously smooth flow to a periodically serrated flow as the cutting speed increases.

Keywords Machining · Titanium alloys · Flow-softening · Finite element analysis · Temperature effects

1 Introduction

Titanium alloy Ti-6Al-4V is a most commonly used material in aerospace and biomedical industries because of its desirable properties including high strength-to-weight ratio, good heat-treatment capability, good bio-compatibility, and resistance to corrosion. However, it is a well-known hard-to-machine material with a very low thermal conductivity that generally gives rise to heat accumulation leading to shear localization in the primary shear zone, and high temperature at the tool-chip interface. Machining of titanium alloys produce undesirable serrated chips which cause large variations in cutting forces and associated vibration which, along with the high rake-face temperature and friction, can severely effect tool life and yield poor dimensional accuracy of the machined part feature [1].

Numerical analysis offers an attractive and cost-effective way for machining process comprehension, reduction of physical test necessary, and optimization of cutting conditions, tool material and tool geometry due to the

---

✉ Jingjing Ji
jijingjing@hust.edu.cn

Kok-Meng Lee
kokmeng.lee@me.gatech.edu

[1] State Key Laboratory of Digital Manufacturing Equipment and Technology (SKL-DMET), School of Mechanical Science and Engineering, Huazhong University of Science and Technology, Wuhan, 430074, Hubei, People's Republic of China

[2] Woodruff School of Mechanical Engineering at Georgia Institute of Technology, Atlanta, GA 30332-0405, USA

poor machinability of titanium alloys. However, a valid material constitutive model that describes the material behavior during the cutting process is needed in finite-element analysis (FEA), which remains a challenge and is a key factor influencing the prediction accuracy, especially in simulating the serrated chip formation [2, 3]. Many material constitutive models have been developed in the past years. Among these, the Johnson-Cook (JC) [4] and Zerilli-Armstrong (ZA) [5] models are widely utilized in modeling and simulation studies and are the representative models for phenomenological and physical-based group respectively. Although the physical-based models are derived from the theory of dislocation dynamics, their parameters cannot be directly measured and thus are generally obtained empirically by curve-fitting the experimental data in a dynamic compression setup such as Taylor impact or Split Hopkinson pressure bar (SHPB) devices [6]. For the same accuracy, models with less parameters are easier to implement in modeling. Even though the dynamic deformation devices provide a material deforming condition close to cutting, the range of the measured strains is limited in most reported experiments, which are well below severe deformation typically encountered in a cutting process. Therefore, as demonstrated in [7], the classical constitutive models, which only taking account the thermal softening of Ti-6Al-4V alloy, were not sufficient to form the special serrated chip and yielded incorrect cutting/thrust forces in FEA simulations. They are only meaningful in certain operation ranges of strains and strain-rates and cannot be extrapolated for uses in high strain and strain-rate conditions. Several modified JC and ZA models have been presented to simulate the serrated chip formation in Ti-6Al-4V machining, which introduce a failure and/or softening term in high strain and can be verified by comparing simulated results with measurable information (including cutting forces, chip morphology, and contact-length) in the cutting experiments. Calamaz et al. [8] introduced a hyperbolic-tangent (tanh) term to augment the JC model for characterizing the flow-softening behavior in high strain condition, which was further modified in [9] and used as a failure function to capture the loss in load bearing capacity related to mirco voids in [10, 11]. However, these modifications have not taken full account the coupled effect of the onset temperature and the critical strain in the dynamic recrystallization (DRX) on flow-softening of Ti-6Al-4V machining.

Although the complicated physical mechanisms responsible for the serrated chip formation when cutting of titanium alloys are still not well understood, it has been commonly accepted that the main reason for adiabatic shear localization is the competition between strain-hardening and thermal-softening, then the thermo-visco-plastic instability and adiabatic shearing results in the formation of serrated chips [8, 12], while others explained this phenomenon by considering initiation and propagation of cracks inside the primary shear zone of the workpiece material [13, 14]. By summarizing a wealth of experimental evidences [15] and analyzing the microstructure and metallurgy evolution of adiabatic shear band (ASB) in terms of cutting speed [16], the researchers found that as the workpiece materials of Ti-6Al-4V alloy was sensitive to adiabatic shearing in machining condition, the mechanism of serrated chip formation was more likely to be attributed to thermoplastic instability. Ye et al. [17] conducted high speed machining of Ti-6Al-4V alloy at a wide range of cutting speeds and the microscopic observations of chips revealed that the transition from continuous chip flow to serrated chip flow can be attributed to repeated shear band formation inside primary shear zone.

By studying the Ti-6Al-4V samples with different microstructures that were subjected to a wide range of strain-rates (10^{-3} to 7000 s^{-1}) and initial temperatures (77 to 1000 K), Nemat-Nasser et al. [18] suggested that flow stress of Ti-6Al-4V was more sensitive to temperature than to strain-rate, and ASBs developed at high strain-rate as well as at low strain-rate with high temperature. Martinez et al. [19] conducted a series of impacting experiments on Ti-6Al-4V targets and the thermally activated DRX microstructure was confirmed by transmission electron microscopy (TEM) analysis within ASB. Moreover, by studying the dynamic deformation behavior of Ti-6Al-4V, Rittel et al. [20] experimentally found that DRX preceded and triggered the ASB failure instead of being its consequence. Jiang et al. [21] reported that the shear bands of deformed pure titanium hat-shaped specimen contained equiaxed ultrafine grains with high-angle boundaries, which should be the products of DRX. Their thermodynamic analysis also revealed that when deforming at strain rate of about 3.2×10^4 s^{-1}, the temperature in the ASB is high enough to meet the requirement of DRX of titanium. As there is an onset temperature for DRX, it should be considered as a coupling critical condition to trigger the ASB, within which the ductile flow-softening failure occurs.

Temperature has a great influence on dynamic deformation behavior of titanium alloys. Chen et al. [22] experimentally found that the deformed specimen and the microstructure of Ti-6Al-4V exhibited different deformation mechanisms around DRX onset temperature (500 °C, suggested by [23]); compression tests conducted below 500 °C generated hardening effect followed by fracture while tests between 500 and 700 °C resulted in flow-softening (or a decrease in hardening) after initial hardening. Germain et al. [24] conducted shear tests on hat-shaped Ti-6Al-4V alloy, the measured force-displacement curves reflected a change in the mechanisms governing the deformation in different temperature range. However, their strain rates were rather low (10 s^{-1}). Based on a series of Ti-6Al-4V cutting experiments (with cutting speeds ranging from 0.05 to 60.58 m/s), Ye et al. [17] further found that the transition from a continuously smooth chip to a periodically serrated chip occurred around a critical cutting speed. In the similar results presented by Wan et al. [25] and He et al. [26] when investigating the machinability of Ti-6Al-4V alloy, machining of Ti-6Al-4V alloy yielded "transitional chip" that nearly segmented chip without adiabatic shear at lower cutting condition, and more segmented and distinct adiabatic shear at higher cutting speed. By investigating the influence of thermal conductivity of Ti-6Al-4V on chip segmentation, the facilitation of serrated chip formation with increasing cutting speed is related to the temperature at the contact tool-chip interface [27]. The above findings suggest that there might be a temperature-dependent "switching" effect on the chip characterization and deformation behavior.

Motivated by published findings, this paper presents an improved JC material constitutive model (referred to here as JCM-IM) to account for the coupled effects of onset temperature and critical strain on flow-softening of Ti-6Al-4V alloy during machining. The remainder of this paper offers the followings:

- We introduce a Gaussian-like temperature dependent factor in the strain-hardening term, which accounts for the flow-softening effect due to the coupling condition of critical strain and onset temperature. As will be shown, this factor mathematically serves as a "bridge" between the classical Johnson-Cook model and its existing modified version, which essentially represents two limiting cases (strain-hardening and flow-softening respectively).
- Along with the procedure for implementing and calibrating the JCM-IM in the machining FEA software, the best-fit parametric values of the JCM-IM for characterizing the Ti-6Al-4V alloy for machining are presented. The calibrated JCM-IM is verified by comparing simulated forces, chip morphology, shear angle, and shear strains in the primary shear band with experimentally measured results. Further validations are presented by comparing with published data over a wide range of Ti-6Al-4V cutting speeds and feed-rates.
- Several sets of simulation results are discussed, which illustrate the effects of cutting speed on the temperature in the friction and shear zones, the chip morphology evolution, and the shear strains in the primary shear zone. As will be shown, the numerical findings intuitively illustrate the transition from a continuously smooth flow to a periodically serrated flow as the cutting speed increases.

2 Material constitutive models

Among the material constitutive models, the Johnson-Cook model (JCM) [4] has been commonly employed for analyzing the material flow stress because of its simple form and numerical robustness. The JCM has the form in Eq. 1a–d where f_{JC}, g and h are the three decoupled functions of the strain ε, strain rate $\dot{\varepsilon}$ and temperature T. These three functions characterize the strain-hardening, strain-rate sensitivity, and thermal-softening respectively:

Johnson-Cook model (JCM):

$$\sigma = f_{JC}(\varepsilon)g(\dot{\varepsilon})h(T) \tag{1a}$$

$$f_{JC}(\varepsilon) = \sigma_A + \sigma_B \varepsilon^n \tag{1b}$$

$$g(\dot{\varepsilon}) = 1 + C \ln \dot{\varepsilon}/\dot{\varepsilon_0} \tag{1c}$$

$$h(T) = 1 - [(T/T_0 - 1)/(T_m/T_0 - 1)]^m \tag{1d}$$

In Eq. 1a–d, $\dot{\varepsilon_0}$ is the reference equivalent plastic strain-rate; T_0 is the room temperature; and T_m is the melting temperature of the workpiece material. The JCM heavily depends on experiments to calibrate its empirical parameters which include the initial yield strength σ_A of the material at room temperature, hardening modulus σ_B, hardening coefficient n, thermal softening coefficient m, and strain-rate sensitivity constant C. SHPB tests (for examples, conducted in [28]) are generally used to calibrate these parameters experimentally, which have limited strains ($<$ 0.35) and strain-rates ($<$ 10^4 s^{-1}) well below severe deformation typically encountered in a machining process (with plastic strains between 100 and 700% and strain-rates up to 10^6 s^{-1}). The JCM is meaningful in certain operating ranges of strains and strain-rates but fails to capture high strain material behavior in machining where the flow stresses cannot be measured by existing standard material testing devices.

2.1 Modified JC material constitutive model

Several correcting functions to account for the temperature effects have recently been proposed to modify the JCM for orthogonal cutting of Ti-6Al-4V alloy. Denoted as $f_{M1}(\varepsilon)$ and $\eta(\varepsilon, T)$ in Eq. 2a, Calamaz et al. [8] proposed two modifications to the JCM; an exponential decay in Eq. 2b to account for strain-softening and a temperature-dependent switching function in Eq. 2c to introduce flow-softening at high strains:

Modified JC Model 1 (JCM-M1):

$$\sigma = f_{M1}(\varepsilon)g(\dot{\varepsilon})h(T)\eta(\varepsilon, T) \tag{2a}$$

$$f_{M1}(\varepsilon) = \sigma_A + \sigma_B \varepsilon^n \exp(-\varepsilon^a) \tag{2b}$$

$$\eta(\varepsilon, T) = 1 - (T/T_m)^d + (T/T_m)^d \tanh^S[\varepsilon + (T/T_m)^b]^{-r} \tag{2c}$$

Four additional parameters (a, b, d and r; S=1) were introduced for calibration. The 5th parameter S (power over the hyperbolic-tangent term) in Eq. 2c was later added by Sima and Özel [9] where the parametric values were empirically tuned in FEA to match the simulated chip morphology and cutting forces with the corresponding experimental data measured when machining Ti-6Al-4V alloy. Using the SHPB test data measured by [28] at high strain-rates and high temperatures and the best-fit model-parameters in Table 1, JCM-M1 successfully simulated the serrated chip formation for adiabatic shearing in machining of Ti-6Al-4V alloy using FEA without damage models, and confirmed the importance of strain-softening phenomenon during chip formation of Ti-6Al-4V. Their results (suggesting that flow-softening is most effective between 300 and 700 °C) agree well with the measured cutting forces (within 5% difference) but exhibit some discrepancies when comparing with the experimental thrust forces (up to 15% difference). However, because of the low value of the best-fit S=0.05, the temperature-dependent function $\eta(\varepsilon, T)$ plays little or no role on the stress-strain curve.

Modified JC Model 2 (JCM-M2):

When the strain, strain-rate, and temperature exceed certain critical values, DRX (defined as the process of microstructure reformation and evolution) results newly crystallized small grains with low dislocation density. Rittel et al. [20] demonstrated that DRX triggers adiabatic shear failure by observing dynamically recrystallized nano-grains in Ti-6Al-4V subjected to impact loading. Schneider et al. [23] estimated that the critical temperature T_r, around which an adiabitic shear band (ASB) was formed, is round 500 °C (773K) or about 0.4T_m (T_m=1933K) for Ti-6Al-4V; and that the recrystallization was not fully driven when the estimated $T < T_r$. In order to characterize the temperature effect on strain-hardening, Chen et al. [22] modified the strain-hardening term in the JCM by introducing a temperature factor:

$$\sigma = f_{M2}(\varepsilon, T) g(\dot{\varepsilon}) h(T) \tag{3a}$$

$$f_{M2}(\varepsilon, T) = \sigma_A + \sigma_B (1 - 0.5T/T_r) \varepsilon^{n_2} \varepsilon^n \tag{3b}$$

$$Q = \frac{\partial \sigma}{\partial \varepsilon} = \sigma_B n \varepsilon^{n-1} \left(1 - \frac{T}{2T_r}\right)^{n_2} g(\dot{\varepsilon}) h(T) \tag{3c}$$

$$Q = \frac{\partial \sigma}{\partial \varepsilon} = \frac{\sigma_i - \sigma_{i-1}}{\varepsilon_i - \varepsilon_{i-1}}, i = 1, 2, \ldots \tag{3d}$$

The corresponding strain-hardening rate Q is defined in Eq. 3c and compared with the experimental data [22] in Fig. 1 where Q was computed incrementally from the slope of the stress-strain curve defined in Eq. 3d. In Fig. 1, the strain-hardening rate Q is normalized to the initial stress defined as $\sigma_0 = \sigma(\varepsilon = 0; \dot{\varepsilon}, T)$.

As observed in Fig. 1, Q decreases rapidly with increasing strain in the low strain region, and then continuously decreases but gradually until reaching a steady value. Similar phenomena can be found in the experimental data [28, 29]. It is worth noting that the experimental Q data decrease below 0 for high temperature conditions (700 °C) and strain-rate higher than 10^4 s^{-1}, suggesting the occurrence of strain softening effect around an onset (critical) temperature. By experimentally reviewing the temperature-dependent microstructure evolution, Chen et al. [22] concluded that the critical temperature for Ti-6Al-4V alloy deformation and microstructure evolution mechanism is about 500 °C, above which the material exhibits higher ductility and formability resulting in flow-softening. JCM-M2 improves the prediction accuracy of the experimental flow stresses over certain temperature and strain-rate ranges. It is meaningful in modeling of the processes with small strain but fail to capture the temperature dependent effect on the flow-softening in large strain for the application of machining modeling. The coupled effect of critical strain and temperature on the flow-softening is illustrated in Fig. 2, where the SHPB test data by [28] and [22] are compared. In Fig. 2, the stress is normalized to the initial stress σ_0; and the experimental stress-strain curves were smoothed by least-square fits so that they are analytically differentiable for deriving the normalized strain-hardening rates (dash-lined in Fig. 2). The critical strain, at which the strain-softening effect is initiated and associated with an onset temperature, is not obvious since the general SHPB test only measures the average strain and stress for the whole specimen and thus

Table 1 Material constants of Ti-6Al-4V constitutive model

JC model parameters

σ_A(MPa)	σ_B(MPa)	C	n	m	$\dot{\varepsilon}_0$	T_0(°C)	T_m(°C)
724.7	683.1	0.035	0.47	1.0	0.01	20	1660

Best-fit JCM-M1 parameters

a	b	d	r	S
2	5	1	1	0.05

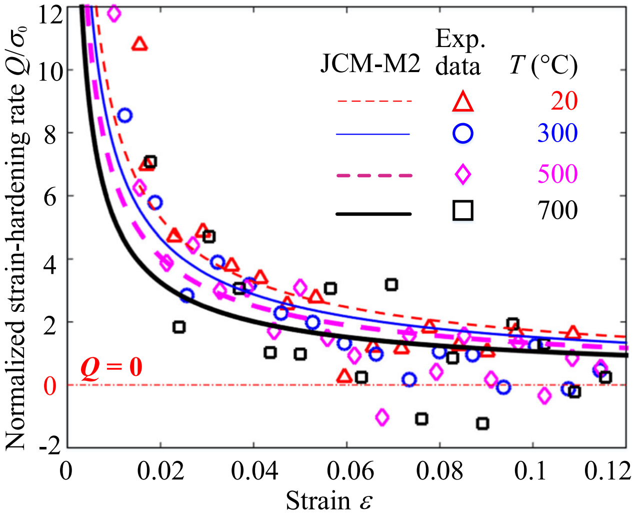

Fig. 1 Normalized strain-hardening rate at different temperature: experimental data [22] and JCM-M2

fails to capture the behavior within the localized ASB where the strain was nearly 10 times of its vicinity [30]. The JCM-M1 and JCM-M2 given in Eqs. 2a–c and Eq. 3a,b generally cannot capture the strong temperature effects on the flow-softening behaviors under large strain range and needed to be further modified.

2.2 Improved JC material constitutive model (JCM-IM)

Motivated by JCM-M1 in Eq. 2a–c to consider the critical strain on flow-softening in large strain range, and by JCM-M2 in Eq. 3a,b to characterize the temperature-dependent effect on deformation behavior around the onset DRX temperature, the improved material constitutive model of Ti-6Al-4V alloy is proposed in Eq. 4a–c. The exponential decay factor in Eq. 2b is modified in Eq. 4b to account for the flow-softening effects due to the coupling condition of critical strain and onset temperature:

$$\sigma = f_I(\varepsilon, T) g(\dot{\varepsilon}) h(T) \tag{4a}$$

$$f_I(\varepsilon, T) = \sigma_A + \sigma_B \varepsilon^n \exp\left[-\frac{(\varepsilon - q)^a}{d}\right] \tag{4b}$$

$$d = \exp\left[\left(\frac{1 - T/T_m}{1 - T_r/T_m}\right)^{a_0}\right] \tag{4c}$$

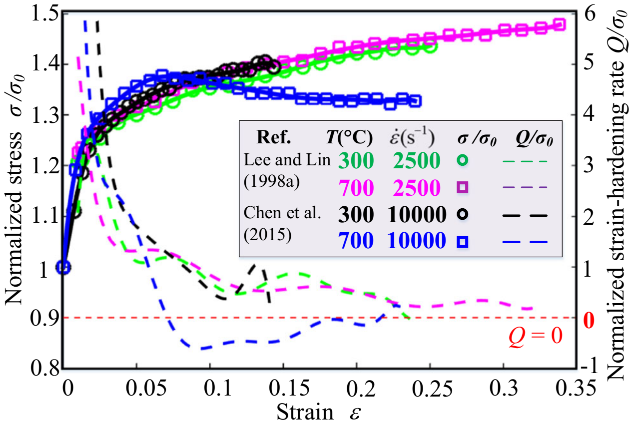

Fig. 2 Normalized stress and strain-hardening rate

The improved strain-hardening function $f_I(\varepsilon, T)$ is defined in Eq. 4b where T_r defined as the critical temperature, above which the flow-softening phenomenon occurs. The modified factor in Eq. 4b is Gaussian-like as illustrated in Fig. 3, where a, q and a_0 characterize the rate of material softening in the shear band, the critical strain that initiates the ASB formation, and the temperature-dependent sensitivity around T_r that triggers the DRX leading to flow-softening, respectively. As temperature increases, the value of the Gaussian-like factor decreases in high strain indicating the occurrence of flow-softening. A lower a_0 value (non-negative) corresponds to a higher temperature-dependent sensitivity of the flow-softening.

The normalized strain-hardening rate is defined as

$$\bar{Q} = \frac{Q}{\sigma_0} = \frac{1}{\sigma_A}\frac{\partial f_I(\varepsilon, T)}{\partial \varepsilon} \tag{5a}$$

$$\frac{\partial f_I}{\partial \varepsilon} = \sigma_B \varepsilon^{n-1}\left[n - \frac{a\varepsilon(\varepsilon - q)^{a-1}}{d}\right]\exp\left[-\frac{(\varepsilon - q)^a}{d}\right] \tag{5b}$$

With two less parameters than Eq. 2a–c, the numerical implementation of JCM-IM is simpler than that of JCM-M1. It is worth noting that JCM and JCM-M1 are two special cases of JCM-IM:

$$f_I = \begin{cases} f_{JC}(\varepsilon), & If\ d \to \infty \quad \text{(JCM)} \\ f_{M1}(\varepsilon), & If\ q = 0, d = 1 \quad \text{(JCM} - \text{M1)} \end{cases} \tag{6}$$

$$\frac{\partial f_I}{\partial \varepsilon} = \begin{cases} \sigma_B \varepsilon^{n-1} n, & If\, d \to \infty \\ \sigma_B \varepsilon^{n-1}(n - a\varepsilon^a)\exp(-\varepsilon^a), & If\, q = 0, d = 1 \end{cases} \tag{7}$$

2.3 Parameter-turning procedure of JCM-IM

The flowchat (Fig. 4a) illustrates the procedure for tuning the JCM-IM coefficients in Eq. 4a–c for orthogonal cutting of Ti-6Al-4V alloy. The machining finite-element modeling (FEM) software AdvantEdge^{TM} (Third Wave Systems, USA), which is based on an updated Lagrangian formulation employing implicit integration method designed for simulating large deformation, is used to simulate the cutting process. The AdvantEdge^{TM} FEM software automatically

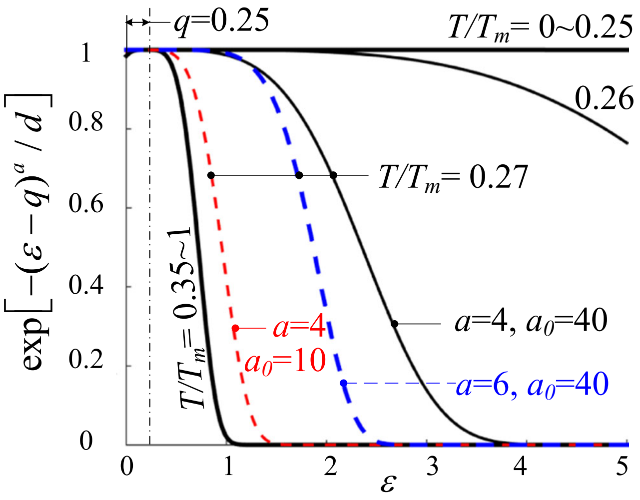

Fig. 3 Parametric effects on the modified exponential decay factor

re-meshes and generates very dense grids near the tool tip so that large gradients of strain, strain-rate and temperature can be handled. Furthermore, a high mesh density is defined around the cutting edge as a moving window to allow continuous and adaptive re-meshing to reduce element distortion and allow for chip separation [31].

For the orthogonal cutting of a Ti-6Al-4V alloy, parameters that specified the cutting condition are feedrate t_u, cutting speed v_c, and tool geometry (Fig. 4b). The JCM-IM (Section 2.2) for the workpiece is implemented in the software via a user-defined yield surface routine coded in FORTRAN. The friction coefficient μ at the tool-chip interface (rake angle α) is modeled by the Coulomb friction law in Eq. 8 where ($\hat{f}_c$, $\hat{f}_t$) are the measured cutting and thrust (feed) forces respectively:

$$\mu = \frac{\hat{f}_t + \hat{f}_c \tan\alpha}{\hat{f}_c - \hat{f}_t \tan\alpha} \tag{8}$$

The primary outputs of the orthogonal cutting simulation are the cutting forces, chip morphology, temperature field, contact length and the shear strains in the primary shear zone as shown in Fig. 4a. The following criteria are used to evaluate the material models. The *1st criterion* is the relative average error defined in Eq. 9 which computes the average difference between the simulated and experimentally measured cutting forces (over N data for two steady-state oscillation cycles):

$$\bar{\mathbf{f}}_{\mathbf{e}} = \begin{bmatrix} \bar{f}_{ec} \\ \bar{f}_{et} \end{bmatrix} = \frac{100\%}{N} \sum_{i=1}^{N} \left| \frac{\mathbf{f_i} - \hat{\mathbf{f}}_{\mathbf{i}}}{\hat{\mathbf{f}}_{\mathbf{i}}} \right| \tag{9}$$

Expressed as % differences in Eq. 10a–b, the *2nd criterion* compares the simulated chip morphology (h_1, h_2, p) with experimentally measured data ($\hat{h}_1$, $\hat{h}_2$, $\hat{p}$) where the maximum and minimum chip thicknesses (h_1, h_2) and serration pitch p are defined in Fig. 4c:

$$\Delta h = \left| \frac{(h_1 - h_2) - (\hat{h}_1 - \hat{h}_2)}{\hat{h}_1 - \hat{h}_2} \right| \times 100\% \tag{10a}$$

$$\Delta p = \left| \frac{p - \hat{p}}{\hat{p}} \right| \times 100\% \tag{10b}$$

The *3rd criterion* bases on the forces (f_c, f_t) calculated by integrating the normal and shear stresses (σ_n, τ_s) along the shear plane with a specific shear angle ϕ:

$$\begin{bmatrix} f_c \\ f_t \end{bmatrix} = w \begin{bmatrix} S_\phi & C_\phi \\ C_\phi & -S_\phi \end{bmatrix} \int_{s=0}^{S} \begin{bmatrix} \sigma_n \\ \tau_s \end{bmatrix} ds \tag{11a}$$

In Eq. 11a, (C_ϕ, S_ϕ) denote (cosϕ, sinϕ); w is the width-of-cut and the shear angle ϕ is defined in Fig. 4d; and the normal and shear stresses (σ_n, τ_s) are defined by the elements of the stress tensor (σ_x, σ_y, τ) of the workpiece material:

$$\begin{bmatrix} \sigma_n \\ \tau_s \end{bmatrix} = \frac{\sigma_x + \sigma_y}{2} \begin{bmatrix} 1 \\ 0 \end{bmatrix} + \frac{\sigma_x - \sigma_y}{2} \begin{bmatrix} -C_{2\phi} \\ S_{2\phi} \end{bmatrix} + \tau \begin{bmatrix} S_{2\phi} \\ C_{2\phi} \end{bmatrix} \tag{11b}$$

The *4th criterion* compares the simulated and measured shear strains in the primary shear band. For a classical

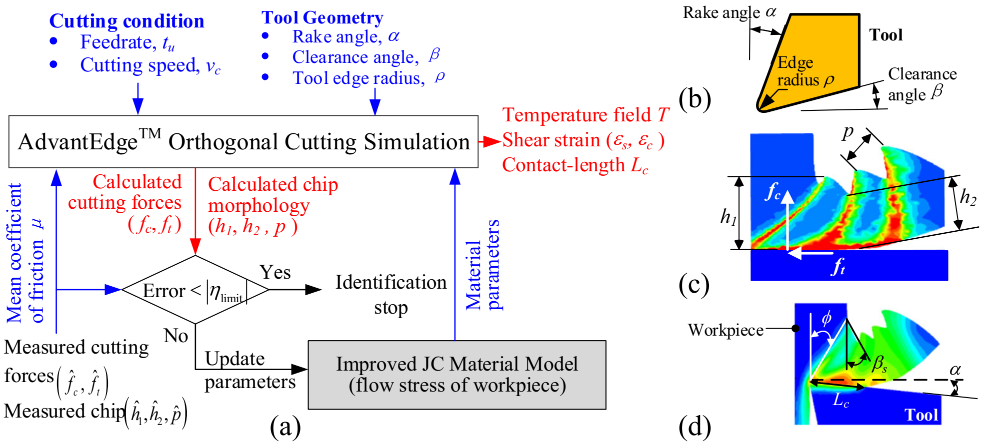

Fig. 4 Constants identification in JCM-IM. **a** Flow chart. **b** Tool geometry. **c** Tuning parameters. **d** Parameters for calculating strain

orthogonal cutting model of continuous chip formation, the overall shear strain ε_s in the primary shear zone and the critical shear strain ε_c that initiates the shear band formation in the serrated chip formation process can be computed from Eq. 12 [32]:

$$\begin{bmatrix} \varepsilon_s \\ \varepsilon_c \end{bmatrix} = \frac{1}{\sin\phi} \begin{bmatrix} \cos\alpha / \cos(\phi-\alpha) \\ \sin\beta_s / \sin(\phi+\beta_s) \end{bmatrix} \tag{12}$$

In Eq. 12, the bulge angle β_s is defined in [32] as the angle between the locations where the serrated formation ends and where the catastrophic shear begins. β_s is shown in Fig. 4d and L_c is the contact length between the chip and cutting tool.

In this study, the two criteria defined in Eqs. 9 and (10a,b) are used to calibrate the coefficients of the JCM-IM.

3 Results and discussions

In this section, cutting experiments were conducted using orthogonal cutting test-bed to validate and verify the proposed JCM-IM by comparing the simulated and experimental results. Four sets of results are presented: The *1st set* determines the unknown parameters for the JCM-IM in Eq. 4a–c. The calibrated models are verified in the *2nd set* by comparing the simulated and measured cutting forces. The *3rd set* validates the JCM-IM by investigating the temperature effects on the serrated chip formation process and by comparing the simulated chip morphology with microscope measured experimental results and published data. The *4th set* investigates the temperature effects on the shear strains in the primary shear zone and the critical conditions that initiates the shear band.

Figure 5 shows the orthogonal experimental setup that includes the machine equipment CK6150A with Siemens 840D NC numerical control system. A thin-wall tube workpiece (Ti-6Al-4V, 120 mm diameter, 1.5 mm thick) rotates about its longitudinal axis while the cutting tool (uncoated tungsten carbide, rake and flank angle is 0° and 11° respectively) is fed in parallel to the rotation axis. A dynamometer Kistler 9257B (measured range: FX: ±5 KN, FY: ±5 KN, FZ: ±10 KN) was used for force signal sensing, where three-directional forces analog signals were exported via current amplifier to three dSPACE A/D channels, and converted into digital signals as output to a desktop computer. The surface temperature was measured by the FLUKE Ti400 infrared thermal imager (resolution

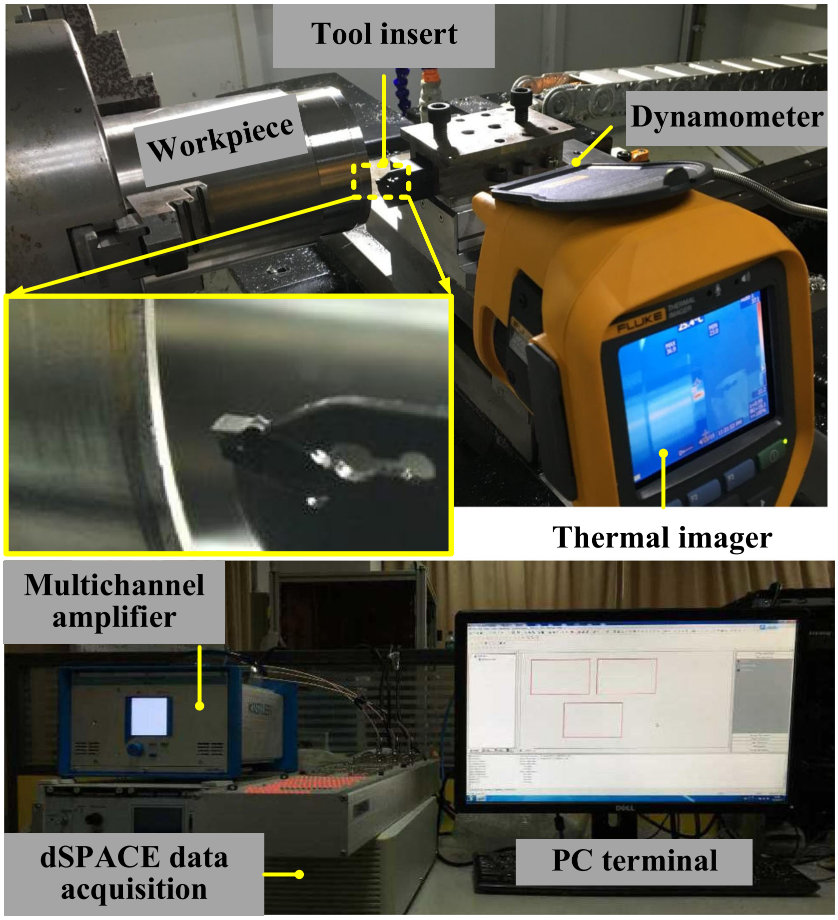

Fig. 5 Orthogonal cutting experimental setup

Table 2 Workpiece and tool material properties

Material properties	Workpiece (Ti-6Al-4V)	Tool insert (WC/Co)
Young modulus E, GPa	113.3	560
Thermal expansion α_t, 1/ °C	7.10×10^{-6}	4.70×10^{-6}
Thermal conductivity λ, W/m/ °C	$7.039\exp(0.0011T)$	55
Specific heat capacity C_p, N/(mm^2 °C)	$2.24\exp(0.0007T)$	$0.0005T + 2.07$
Density ρ, kg/m^3	4,430	14,000
Poison's ratio	0.342	0.232

320×240 pixels, 9 Hz) providing a spatial resolution of 250 µm/pixel with a minimum focus distance of 15 cm.

In the FEM simulations, the cutting tool was modeled as a rigid body with a mesh containing 2,000 elements (with minimum element size limited to 20 µm); and the workpiece was modeled using triangular elements with size ranging from 2 to 10 µm. The material properties of workpiece and tool used in the simulation are listed in Table 2 where the temperature-dependent material properties were applied in the AdvantEdge through a data table.

3.1 Parameter tuning of JCM-IM

In order to study the effects of the JCM-IM parameters (a, a_o, q and T_r) on the cutting and thrust forces, several sets of parametric values (summarized in Table 3) were used in the simulations. The published best-fit parametric values [9] for the JCM-M1 (Table 1) were used as initial values to tune the JCM-IM in Eq. 4a–c. All cases were simulated with the same cutting conditions listed in Table 3 (first row). The results are presented in Table 3 and Fig. 6.

Some observations can be made from the comparison of results:

- As shown in Fig. 6, Case 1 and JCM-M1 yield nearly identical forces when the best-fit parameters (q=0 and a=2 in Table 1) suggested in [9] for JCM-M1 are used. T_r was chosen to be 20 °C (room temperature) indicating that the occurrence of flow-softening is decided primary by critical strain. An initial value of 40 was chosen for a_0 to guarantee a medium sensitivity around T_r.
- The comparisons between Case 3 and Case 1 show that the introduction of T_r=500 °C improves the thrust force prediction. This observation is consistent with that reported in [33] where the thrust force prediction was reportedly improved when temperature dependent flow-softening was introduced with a critical temperature of 350 °C. Also, the T_r value was found to affect the serrated chip morphology significantly, reducing the relative difference by more than 10% from Case 1 (36.2%, 24.7%) to Case 3 (22.5%, 14.3%).

Table 3 Parametric values used in eleven cases of simulations

Case	(a, T_r, q, a_0)	Simulation (f_c, f_t)N/m	Relative error (f_c, f_t)%	Relative error $(\triangle h, \triangle p)$%
1	(2, 20, 0, 40)	(219.0, 83.4)	(2.66, 10.01)	(36.2, 24.7)
2	(2, 350, 0 , 40)	(232.7, 86.9)	(3.40, 6.23)	(36.1, 20.1)
3	(2, 500, 0, 40)	(236.7, 94.9)	(5.18, 2.35)	(*22.5*, 14.3)
4	(2, 500, 0.3, 40)	(245.6, 99.1)	(9.14, 6.86)	(37.5, *13.7*)
5	(2, 500, – 0.1, 40)	(238.1, 93.8)	(5.83, 1.12)	(25.2, 75.5)
6	(4, 500, 0, 40)	(231.3 , 93.8)	(2.81, 1.15)	(26.6, 16.9)
7	(4, 500, 0.25, 40)	(240.3, 97.6)	(6.77, 5.22)	(32.1, 16.2)
8	(4, 500, 0.5, 40)	(252.3, 102)	(12.10, 10.15)	(36.2, 15.7)
9	(4, 500, – 0.25, 40)	(229.2, 92.1)	(1.88, *0.63*)	(25.6, 16.1)
10	(4, 500, – 0.25, 20)	(228.8, 94.0)	(*1.69*, 1.38)	(25.2, 16.8)
11	(4, 500, – 0.25, 10)	(221.1, 89.3)	(1.74, 3.68)	(30.7, 16.9)

Tool geometry: $(\alpha, \beta, \rho) = (0°, 11°, 5\ \mu m)$

Cutting condition: $(v_c, t_u) = (2\ m/s, 127\ \mu m/rev)$

Experimental cutting forces: $(\hat{f_c}, \hat{f_t}) = (225.01, 92.72)$ N/m

Friction coefficient: $\mu = 0.4121$

Experimental chip morphology $(\hat{h_1}, \hat{h_2}, \hat{p}) = (177, 104, 90)$ µm

Note: The lowest relative errors among all cases are shown in italics

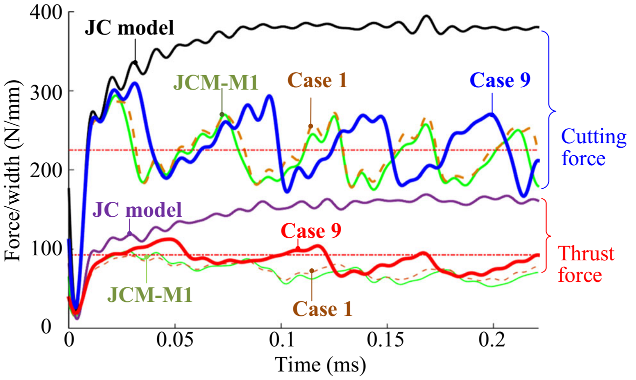

Fig. 6 Comparison of predicted forces with specified experimental values

- The value of q has a notable influence on both cutting and thrust force predictions; q also influences the chip thickness prediction without significantly changing the serration pitch.
- By varying a, the effect on the cutting force is more obvious than on the thrust force (Case 6 and Case 3); and has little effects on chip morphology prediction.
- Decreasing the value of a_o causes little changes (Case 10 and Case 11), but further reducing the value resulting in lower cutting and thrust forces.

These findings suggest that the critical strain (dictated by q and a) and critical temperature T_r have strong influences on the simulated forces and on the serrated chip morphology. By considering the cutting/thrust forces and the chip morphology, the parametric values in Case 9 are considered as a best-fit for the JCM-IM and used throughout in the subsequent simulations.

In addition to the cutting/thrust forces and chip morphology, the tool-chip contact-length L_c of the orthogonal cutting process can be numerically simulated with the calibrated JCM-IM (Case 9). As shown in Fig. 7, the simulated contact-length in the serrated chip formation process is time-periodic with a frequency similar to that of the cutting force f_c. The simulation using JCM-IM predicts the contact-length reasonably well when comparing its maximum with the experimental measured result, which was obtained by inspecting the tool wear on the rake face of the used insert from microscopy image. The contact-length at the tool-chip interface, which can be obtained from high-fidelity simulation with JCM-IM, provides essential boundary condition for reconstructing the temperature distribution of the cutting tool [34].

3.2 Validation and comparison of material models

Using the constitutive material models in Section 2, the normalized strain-hardening rate (Q/σ_0) defined in Eq. 5a and the stress-strain relation at different temperatures were computed for three versions of models in Figs. 8a and 9a,b respectively. In Fig. 8a, the negative strain-hardening rate (below the red dotted-line $Q = 0$) indicates the occurrence of flow-softening. Figure 8b and c are published images [22] showing the experimentally captured cross-sections of the specimens deformed at strain-rate of 10^4 s^{-1} and different temperatures of 300 and 700 °C, which reveal two different deformation mechanisms in the ASB due to the temperature effects: At low temperature (300 °C), the generated strain-hardening results in cracks; At high temperature (700 °C), the localized ASBs are formed with large deformation but with no obvious crack, within which flow-softening is considered to occur. In Fig. 9a, the normalized strain-hardening rates calculated using the JCM and JCM-M1 are compared with published experimental data (Fig. 1) and the enhanced Zerilli-Armstrong (ZA) model [11]; the latter was proposed to account for the strain-rate dependent effects on the material flow strength during the shear band formation. Figure 9b shows the temperature effects on the flow stress predicted by the JCM-IM.

Some observations are drawn from Figs. 8a–c and 9a,b:

- All the models agree well with each other and with experimental data in the low-strain range (< 0.35), but exhibit different trends in the high-strain range.
- As shown in Figs. 8a and 9a, the JCM and JCM-M1 do not account for flow-softening due to the temperature effect, the JCM assumes strain-hardening ($Q > 0$) throughout all the temperature conditions whereas the JCM-M1 triggers flow-softening after the critical strain for all temperatures.
- As graphically compared in Fig. 9a, the enhanced ZA model underestimates the temperature effects on the flow stress curves.
- Built upon published experimental findings and numerical analyses, the JCM-IM is capable of predicting different deformation mechanisms around the DRX with the onset temperature (500 °C). The improved strain-hardening function $f_I(\varepsilon, T)$ defined in Eq. 4b accounts for the temperature effects on flow-softening, and mathematically serves as a “bridge” between the JCM and the JCM-M1, which essentially represents two limiting (strain-hardening and flow-softening) cases of the JCM-IM as intuitively illustrated in Figs. 8a and 9b.

3.3 Model verification for orthogonal cutting of Ti-6Al-4V alloy

The JCM-IM has been verified by comparing the simulated forces, chip morphology and shear strain in the primary shear zone with the experimentally measured data from Ti-6Al-4V dry orthogonal cutting in Fig. 5. More published

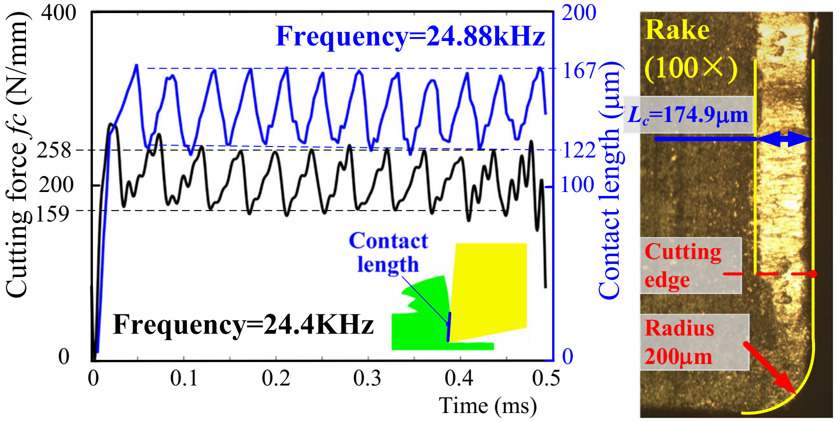

Fig. 7 Simulation results of periodic cutting force and contact length at v_c=2 m/s and t_u=100 μm/rev

experimental data [17, 32] are cited to further validate the effectiveness of JCM-IM for predicting the cutting forces and chip morphology over a wide range of cutting speeds.

3.3.1 Cutting forces

The cutting/thrust forces simulated using the JCM-IM are compared with experimental measurements in Table 4, where the experimental forces were measured by a dynamometer for a range of cutting conditions in Fig. 5. For ease of visualization, the errors defined in Eq. 9 for the forces (simulated with the JCM-IM) are graphed in Fig. 10a at four feed-rates (25, 50, 75, 100 μm/rev) with cutting speed of 2 and 4 m/s respectively. To provide a basis for analyzing the temperature effects, Fig. 10b–d graph the different shear angles and stresses under one of the cutting conditions that simulated using JCM-IM and JCM-M1 respectively. Published data [32] are used as an

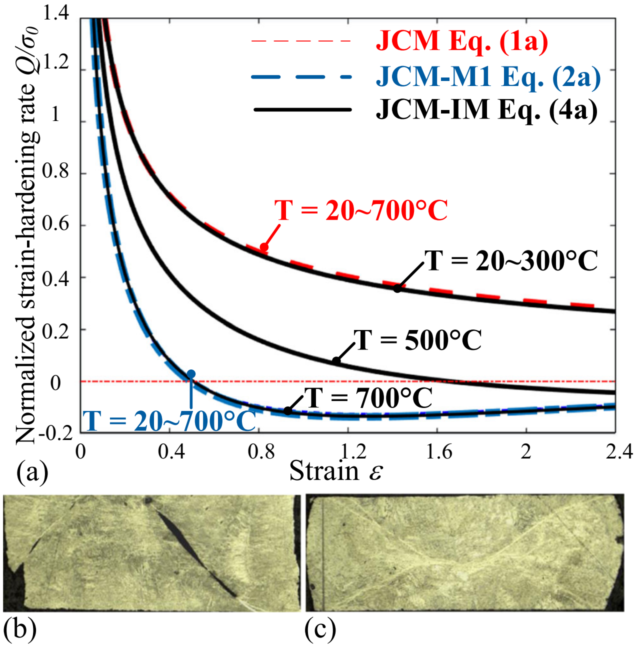

Fig. 8 **a** Comparison of normalized strain-hardening rates calculated by different models. **b** Deformed specimen at 300 °C. **c** Deformed specimen at 700 °C

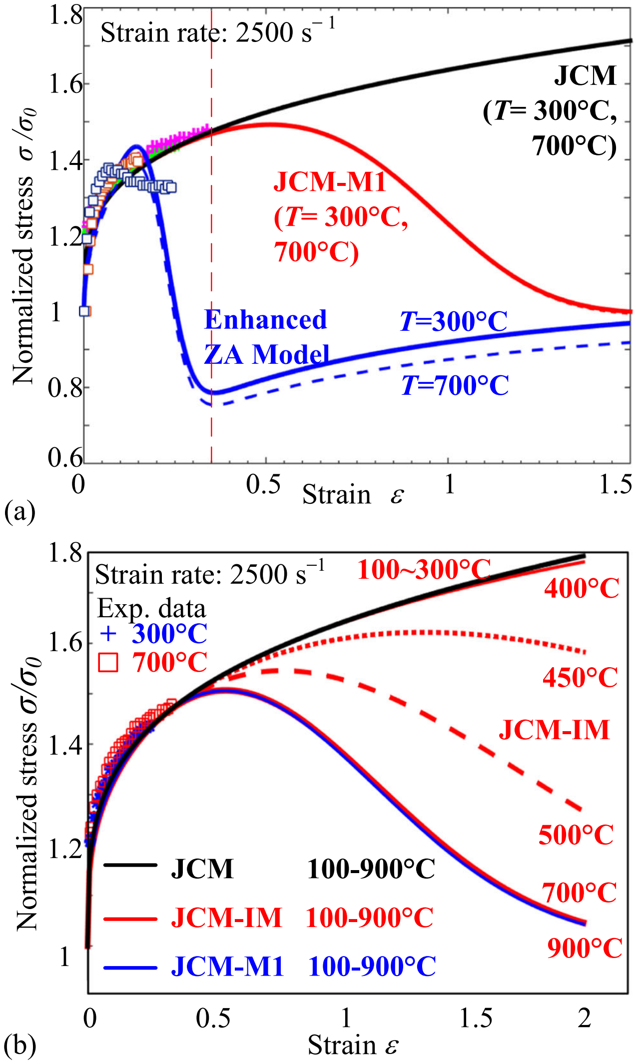

Fig. 9 Normalized flow stress-strain curves as a function of temperature. **a** JCM [4], JCM-M1 [9], and enhanced ZA model [11]. **b** JCM-IM and experimental data from [28]

Table 4 Comparison of simulated and experimental measured forces at different cutting conditions

Feed rate, t_u (µm/r)	(f_c, f_t) N/m at 0° rake angle			
	Experimental		Simulated	
	$v_c = 2m/s$	$v_c = 4m/s$	$v_c = 2m/s$	$v_c = 4m/s$
25	61.1, 43.5	60.5, 40.3	60.1, 40.2	59.5, 37.0
50	106.6, 53.9	102.3, 51.3	108.2, 51.6	103.9, 48.9
75	147.6, 65.3	143.6, 63.6	146.0, 62.7	143.1, 59.0
100	180.4, 76.0	176.4, 72.1	182.7, 73.8	176.2, 68.3

additional basis for comparisons to verify the JCM-IM on the cutting/thrust force predictions at low cutting speeds. The uncoated WC inserts (ISO code M25-M40 / K20-K30) were used throughout the published experiments, the cutting forces were measured for the tool geometry ($\rho = 5 \sim 8$µm and $\alpha = 6.5°$). In our simulations, the tool parameters ($\rho = 5$µm, $\alpha = 6.5°$ and $\beta = 11°$) were used and the simulated forces in each data set (cutting speed of 1/6, 1/3, 2/3, 1, 4/3 and 2 m/s) were curve-fit for comparing with the published data. The results are presented in Fig. 11.

The results for model verification based on force comparisons are summarized below:

- Figure 10a demonstrates that, JCM-IM improves the thrust force f_t prediction and accurately predicts the cutting force f_c for four feed-rates and two cutting speeds. The simulated f_c and f_t are within 2 and 8% errors respectively as compared to 15% discrepancy with JCM-M1 reported in [9].
- The underestimation of the simulated thrust force f_t with the experimental measurements in Table 4 and Fig. 10a were commonly reported in published literatures [8, 9]. As graphed in Fig. 10b, the workpiece flowed against the tool, and was heated in the plastic deformation process. The workpiece material experienced a combination of cool deforming and hot deforming processes during cutting. As shown in Fig. 9b, the material behaviors described by JCM-IM and JCM-M1 matched well with each other above the critical temperature but exhibited different trends in the low-temperature range. The shear angle that simulated using JCM-IM in Fig. 10b is found to be lower than JCM-M1 indicating more hardening effect in the cutting process. The improvement of the thrust force can be explained with the aid of Fig. 10c,d. As shown in Fig. 10c, the stresses along the shear plane can be extracted from the finite-element simulation results using JCM-IM and JCM-M1 respectively. And the pressures along cutting and feed direction can be calculated by Eq. 11a without integration. As shown in Fig. 10d, the predicted thrust force by JCM-IM improves while the cutting force remains nearly the same. As suggested in [11], the predictions can be further improved with finer adjustments of friction regions and their values.

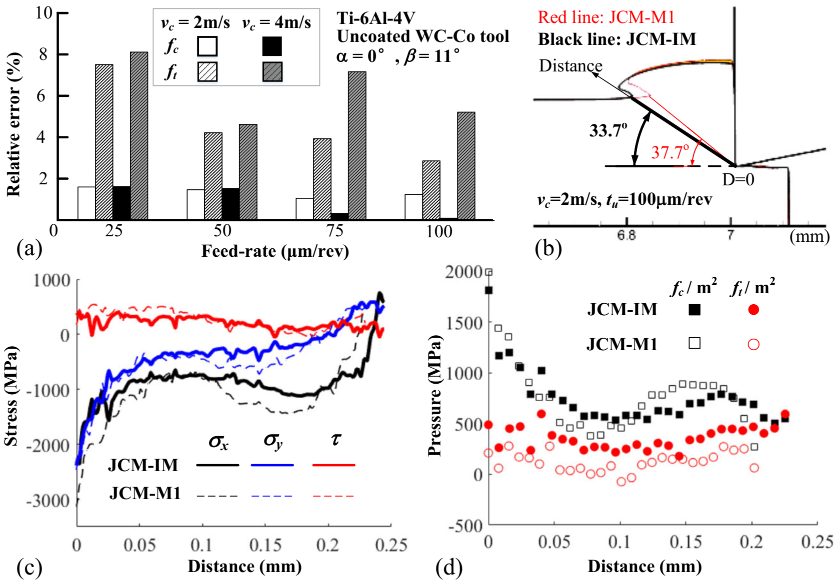

Fig. 10 Comparison of **a** experimental measured and simulated forces using JCM-IM, **b** simulated shear angles using JCM-IM and JCM-M1 respectively, **c** simulated stresses, and **d** calculated cutting/feed pressures along shear plane

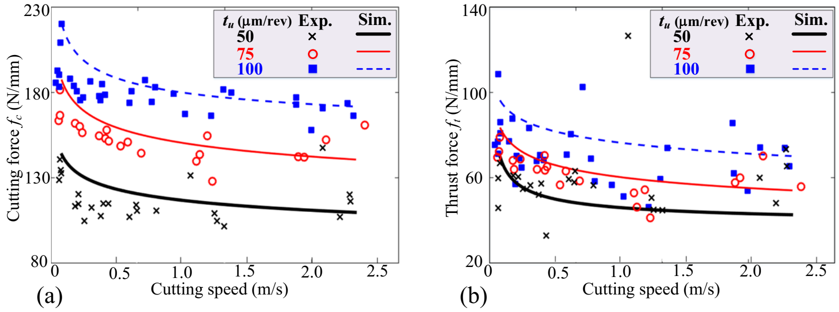

Fig. 11 Comparison between the JCM-IM simulations and experimental data from [32]. **a** Cutting forces. **b** Thrust forces

- The simulation results show that the forces decrease rapidly in the low v_c range, and continue to decrease but gradually become flat over the high v_c range, which agree well with experiments. And this trend is commonly reported in cutting experiments [35]. The observations suggest that the material transforms its deforming behavior from flow-hardening to flow-softening around a critical cutting condition.

3.3.2 Temperature effects on chip morphology evolution

The comparisons between the simulated and experimental measured chip morphology are summarized in Table 5, where the experimental results were observed by an optical microscope after embedding the cutting chips into epoxy resin at different cutting conditions. The chip morphology was simulated by implementing the constitutive material model for different cutting conditions with material properties in Table 2.

Published experimental results [17] of Ti-6Al-4V alloy cutting (Fig. 12) are used to further validate the simulations on chip morphology evolution over wide ranges of cutting speeds. Ye et al. [17] suggests that there is an onset cutting speed for the serrated chip formation. Arrazola et al. [1] and Wan et al. [16] presented similar results when analyzing the chip morphology at different cutting speeds. These consistent findings that the chip morphology evolves from continuous chip, incipient aperiodic serrated chip, and finally to periodic serrated chip with increasing cutting speed, offer further measurable information for model validation.

Table 5 Characteristic parameters of chip morphology at cutting speed of 2 m/s with different feed-rates

Feed-rate(μm/rev)	Exp.($\hat{h}_1$, $\hat{h}_2$, $\hat{p}$)(μm)	Sim.(h_1, h_2, p)(μm)
25	(40.5, 26.5, 19.3)	(41.6, 32.5, 14.1)
50	(81.3, 58.2, 35.1)	(79.1, 66.9, 33.6)
75	(150.5, 92.7, 64.0)	(138.1, 86.1, 60.2)
100	(158.8, 95.5, 72.2)	(150.8, 99.2, 67.2)

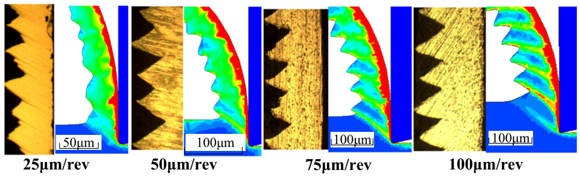

The results are compared in Fig. 12 where the three columns correspond to the cutting speeds for which the three material models are compared: 0.05 m/s (1st column), 0.51 m/s (2nd column), and 4.07 m/s (3rd column). The first row (Fig. 12) compares the published cross-sectional images [17] of the chips for the three cutting speeds, which were captured by microscopic observations after mechanically polished and etched. The next three rows compare the strain fields simulated using the three different material models: JCM (2nd row), JCM-M1 (3rd row) and JCM-IM (4th row). The last row shows the effects of increasing speeds on the temperature fields and serrated chip formation computed with the JCM-IM, and also graphs the contact-length L_c which decreases as the cutting speed increases.

Some observations can be made from Table 5 and Fig. 12:

- As listed in Table 5, JCM-IM simulations at moderate cutting speed of 2 m/s with four feed rates show reasonable accuracy as compared to the experimental measurements.
- As shown in Fig. 12, the experimental images (1st row) show that there exists a distinct transition from continuously smooth flow at lower speeds to periodically serrated flow with the increased cutting speeds. As revealed in the last row, the critical cutting speed corresponding to such transition exhibits a strong temperature dependency for the Ti-6Al-4V alloy.
- At the low speed of 0.05 m/s, the highest temperatures occur in both the friction zone (tool-chip interface) and the shear zone but are lower than the critical temperature ($T_r = 500°C$). As noted in [17], the chip flow is smooth, and the flow motion is homogenous as all crystal particles are elongated uniformly along a direction.
- As the cutting speed increases to 0.51 m/s, the highest temperature in the friction zone increases above T_r whereas that in the shear zone remains below.

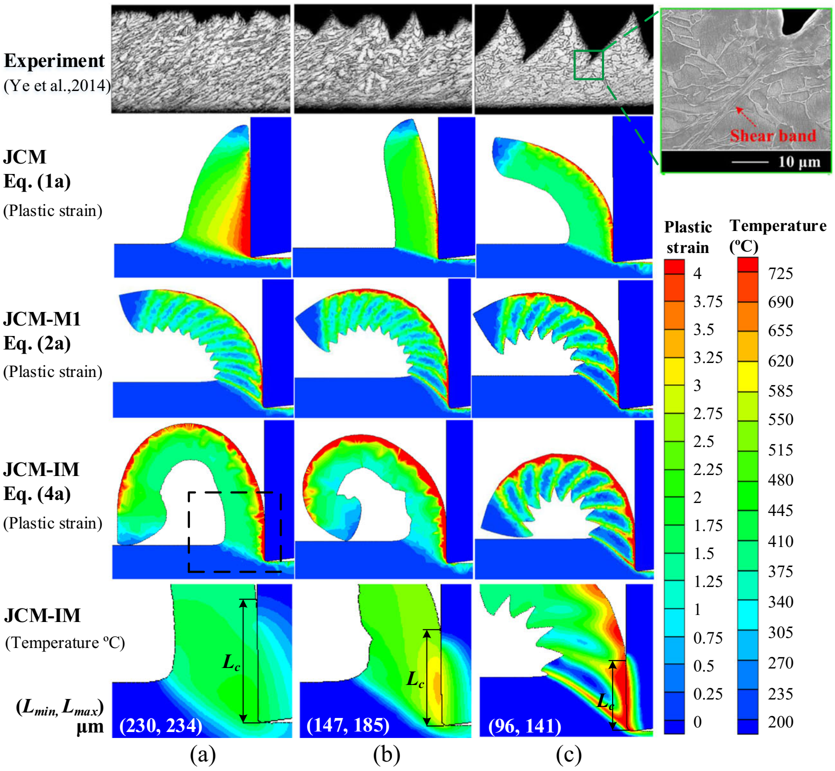

Fig. 12 Chip morphology evolution with increasing cutting speeds at 100 µm feed-rate for $\alpha = 0°$: (**a**) 0.05 m/s, (**b**) 0.51 m/s, and (**c**) 4.07 m/s

- At the high speed of 4.07 m/s, the highest temperatures in both the shear and friction zones increase above T_r. As seen in the image, highly localized shear bands emerge because the smooth chip flow is insufficient to dissipate the energy through homogeneous plastic flow, which cause the steady chip flow to break resulting in a serrated chip flow formation.
- The comparison between the simulation results (2nd to 4th rows) and experimental captured images (1st row) shows that the chip morphology simulated with JCM has a continuously smooth form with no ASB, but that simulated with JCM-M1 is characterized by the widely observed saw-teeth serrated formation with ASB in all three cases of cutting speeds. The simulated chip morphology with JCM-IM agrees well with the experimentally observed patterns that evolve with cutting speed. These findings confirm the effectiveness of the improved function $f_I(\epsilon, T)$ defined in Eq. 4b to characterize the evolution of the chip flow pattern and the ASB.

3.3.3 Effects of cutting temperature on shear band

Using a close-up lens, the surface temperature distribution around the shear band can be captured in the orthogonal cutting (Fig. 5). An infrared image of steady-state with specified cutting conditions ($v_c = 0.067$ m/s, $t_u = 100$ µm/rev) and tool geometry ($\rho = 5$µm, $\alpha = 6.5°$, $\beta = 11°$) is shown in Fig. 13a, where the edges of the tool, workpiece and chip were outlined by solid black lines. The shear plane of the orthogonal cutting can be experimental determined by calculating the second-order gradient along the Y (vertical) direction, indicating the shear deformation heat source, and shown in top-right of Fig. 13a. Simulations under the same cutting conditions and tool geometry were conducted using JCM-IM (bottom-right in Fig. 13a) with the material properties in Table 2. The simulated shear angle ϕ is found to be 22°, which agrees well with the experimental measured result.

With the simulated chip morphology, the overall shear strain ε_s in the primary shear zone and the critical shear ε_c to initiate shear band formation in the serrated chip formation process are calculated from Eq. 12 and compared with published data [32] in Fig. 13b for the same tool geometry, cutting conditions and materials used in Fig. 11. Figure 13b shows that the plots of ε_s and ε_c exhibit similar trends as the forces simulated in Fig. 11, which decrease rapidly at low speeds approaching their near-constant values at high cutting speeds.

To provide a basis to analyze the effects of cutting speeds on the temperature and shear strain in the primary shear band, the temperature data were extracted along the shear plane. The results are summarized in Fig. 13c, d where x_s is the displacement measured from the tool tip along the primary shear band; and the color legends for the temperature and strain fields are the same as Fig. 12.

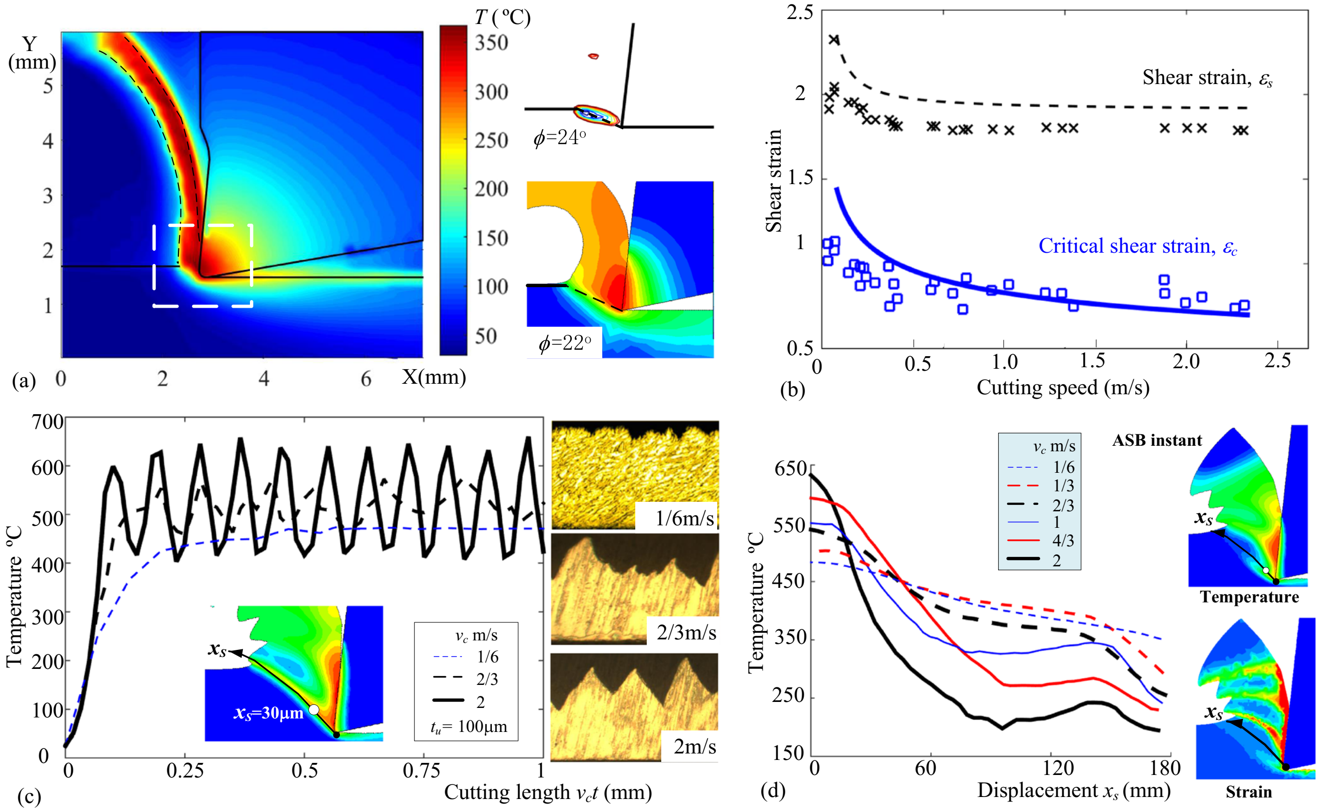

Fig. 13 Effects of cutting speeds on the shear strain and temperature in the shear band: **a** experimental captured temperature distribution near the shear band, and experimental calculated and simulated shear angles; **b** shear strains, experimental data taken from [32], simulated fit-curve by the JCM-IM; **c** temperature evolvement at x_s=30 μm; and **d** $T(x_s)$ at ASB instant

Figure 13c displays the temperature $T(t)$ at x_s=30 μm for three different cutting speeds (v_c=1/6, 2/3 and 2 m/s). Figure 13d graph the temperature T along x_s at instant when segment formation ends and adiabatic shear begins (shown on the right of Fig. 13d) for six different cutting speeds. As illustrated in Fig. 13c,d, $T(x_s, t)$ evolve from a continuously smooth profile (v_c=1/6 m/s) to a periodic curve (v_c=2 m/s); the transition occurs around a critical temperature of T_r = 500°C which corresponds to a critical speed of v_c=2/3 m/s for the 100 μm feed-rate cutting.

4 Conclusion

An improved JC constitutive material model (JCM-IM) capable of predicting different deformation behaviors around the primary shear zone for machining Ti-6Al-4V alloy has been presented. This new model integrates a Gaussian-like temperature dependent factor in the strain hardening term, which effectively relaxes a common assumption that neglects the coupling effect of the critical strain and onset temperature on flow-softening. The JCM-IM has been implemented in the machining FEA software AdvantEdge, and calibrated. The JCM-IM has been verified by comparing the simulated forces, chip morphology, shear angle and shear strains in the primary shear band with experimental measurements and published data over a wide range of Ti-6Al-4V cutting conditions.

Comparisons between simulations with experimental results show that the JCM-IM accurately predicts the cutting forces (within 2% error) for a range of feed-rates (25 to 100 μm/rev) at two cutting speeds (2 and 4 m/s) with rake-angle of 0°. The JCM-IM also improves the predictions (within 8% errors) of the thrust forces for all feed-rates and speeds. The simulations of cutting and thrust forces using JCM-IM presented the similar trend with experimental results over a wide range of cutting speeds. A distinct transition from a continuously smooth flow (low speeds) to a periodically serrated flow (high speeds) can be observed numerically from the simulated chip morphology which agree well with the experimental microscopic observations and are consistent with the simulated temperature fields and shear-strains. The transition was found to occur around a critical temperature of 500 °C which corresponds to a critical cutting speed of 2/3 m/s for the 100 μm feed-rate cutting.

Our research findings confirm the importance of temperature effect on the material deformation behavior of Ti-6Al-4V alloy. The coupled effect of critical strain and temperature on flow-softening has a strong influence on the cutting/thrust forces and chip morphology. As demonstrated numerically, the temperature-dependent factor mathematically serves as a "bridge" between the classical JCM and its existing modified version (JCM-M1), which essentially represents two limiting (strain-hardening and flow-softening) cases of the JCM-IM.

Funding information This work was partially supported by the National Natural Science Foundation of China [No. 51505168]; the U.S. National Science Foundation [No. CMMI-1662700]; and the National Basic Research Program of China [No. 2013CB035803].

References

1. Arrazola PJ, Garay A, Iriarte LM, Armendia M, Marya S, Maître FL (2009) Machinability of titanium alloys (Ti6Al4V and Ti555.3). J Mater Process Technol 209:2223–2230
2. Sadeghifar M, Sedaghati R, Jomaa W, Songmene V (2018) A comprehensive review of finite element modeling of orthogonal machining process: chip formation and surface integrity predictions. Int J Adv Manuf Technol. https://doi.org/10.1007/s00170-018-1759-6
3. Arrazola PJ, Özel T, Umbrello D, Davies M, Javwhir IS (2013) Recent advances in modelling of metal machining processes. CIRP Ann - Manuf Technol 62:695–718
4. Johnson GR, Cook WH (1983) A constitutive model and data for metals subjected to large strains, high strain rates and high temperatures. In: Proc. 7th Int. Symp. Ballist. The Hague, pp 541–547
5. Zerilli FJ, Armstrong RW (1987) Dislocation-mechanics-based constitutive relations for material dynamics calculations. J Appl Phys 61:1816–1825
6. Yu J, Jiang F, Rong Y, Xie H (2014) Numerical study the flow stress in the machining process. Int J Adv Manuf Technol 74:509–517
7. Ducobu F, Rivière-Lorphèvre E, Filippi E (2014) Numerical contribution to the comprehension of saw-toothed Ti6Al4V chip formation in orthogonal cutting. Int J Mech Sci 81:77–87
8. Calamaz M, Coupard D, Girot F (2008) A new material model for 2D numerical simulation of serrated chip formation when machining titanium alloy Ti-6Al-4V. Int J Mach Tools Manuf 48:275–288
9. Sima M, Özel T (2010) Modified material constitutive models for serrated chip formation simulations and experimental validation in machining of titanium alloy Ti-6Al-4V. Int J Mach Tools Manuf 50:943–960
10. Che J, Zhou T, Liang Z, Wu J, Wang X (2018) Serrated chip formation mechanism analysis using a modified model based on the material defect theory in machining Ti-6Al-4 V alloy. Int J Adv Manuf Technol. https://doi.org/10.1007/s00170-018-1787-2
11. Liu R, Melkote S, Pucha R, Morehouse J (2013) An enhanced constitutive material model for machining of Ti–6Al–4V alloy. J Mater Process Technol 213:2238–2246
12. Calamaz M, Coupard D, Nouari M, Girot F (2011) Numerical analysis of chip formation and shear localisation processes in machining the Ti-6Al-4V titanium alloy. Int J Adv Manuf Technol 52:887–895
13. Chen G, Ren C, Yang X, Jin X, Guo T (2011) Finite element simulation of high-speed machining of titanium alloy (Ti-6Al-4V) based on ductile failure model. Int J Adv Manuf Technol 56:1027–1038
14. Yaich M, Ayed Y, Bouaziz Z, Germain G (2017) Numerical analysis of constitutive coefficients effects on FE simulation of the 2D orthogonal cutting process: application to the Ti6Al4V. Int J Adv Manuf Technol 93:283–303
15. Dodd B, Bai Y (2012) Adiabatic shear localization: frontiers and advances. Elsevier
16. Wan ZP, Zhu YE, Liu HW, Tang Y (2012) Microstructure evolution of adiabatic shear bands and mechanisms of saw-tooth chip formation in machining Ti6Al4V. Mater Sci Eng A 531:155–163
17. Ye GG, Chen Y, Xue SF, Dai LH (2014) Critical cutting speed for onset of serrated chip flow in high speed machining. Int J Mach Tools Manuf 86:18–33
18. Nemat-Nasser S, Guo WG, Nesterenko VF, Indrakanti SS, Gu YB (2001) Dynamic response of conventional and hot isostatically pressed Ti-6Al-4V alloys: experiments and modeling. Mech Mater 33:425–439
19. Martinez F, Murr LE, Ramirez A, Lopez MI, Gaytan SM (2007) Dynamic deformation and adiabatic shear microstructures associated with ballistic plug formation and fracture in Ti-6Al-4V targets. Mater Sci Eng A 454:581–589
20. Rittel D, Landau P, Venkert A (2008) Dynamic recrystallization as a potential cause for adiabatic shear failure. Phys Rev Lett 101:165501
21. Jiang Y, Chen Z, Zhan C, Chen T, Wang R, Liu C (2015) Adiabatic shear localization in pure titanium deformed by dynamic loading: Microstructure and microtexture characteristic. Mater Sci Eng A 640:436–442
22. Chen G, Ren C, Qin X, Li J (2015) Temperature dependent work hardening in Ti-6Al-4V alloy over large temperature and strain rate ranges: experiments and constitutive modeling. Mater Des 83:598–610
23. Schneider J, Dong L, Howe JY, Meyer HM (2011) Microstructural characterization of Ti-6Al-4V metal chips by focused ion beam and transmission electron microscopy. Metall Mater Trans A Phys Metall Mater Sci 42:3527–3533
24. Germain G, Morel A, Braham-Bouchnak T (2013) Identification of material constitutive laws representative of machining conditions for two titanium alloys: Ti6Al4V and Ti555-3. J Eng Mater Technol 135:31002–1
25. Wan L, Wang D, Gao Y (2016) The investigation of mechanism of serrated chip formation under different cutting speeds. Int J Adv Manuf Technol 82:951–959
26. He L, Su H, Xu J, Zhang L (2018) Simulation analysis of the influence of dynamic flow stress behavior on chip formation. Int J Adv Manuf Technol 95:2301–2313
27. Zang J, Zhao J, Li A, Pang J (2017) Serrated chip formation mechanism analysis for machining of titanium alloy Ti-6Al-4V based on thermal property. Int J Adv Manuf Technol 2:1–9
28. Lee WS, Lin CF (1998) Plastic deformation and fracture behaviour of Ti-6Al-4V alloy loaded with high strain rate under various temperatures. Mater Sci Eng A 241:48–59
29. Lee WS, Lin CF (1998) High-temperature deformation behaviour of Ti6Al4V alloy evaluated by high strain-rate compression tests. J Mater Process Technol 75:127–136
30. Wright TW (2002) The physics and mathematics of adiabatic shear bands. Cambridge University Press

31. Marusich TD, Ortiz M (1995) Modelling and simulation of high-speed machining. Int J Numer Methods Eng 38:3675–3694
32. Cotterell M, Byrne G (2008) Dynamics of chip formation during orthogonal cutting of titanium alloy Ti-6Al-4V. CIRP Ann - Manuf Technol 57:93–96
33. Karpat Y (2011) Temperature dependent flow softening of titanium alloy Ti6Al4V: an investigation using finite element simulation of machining. J Mater Process Technol 211:737–749
34. Ji J, Huang Y, Lee K-M (2017) A hybrid method based on macro-micro modeling and infrared imaging for tool temperature reconstruction in dry turning. IEEE/ASME Trans Mechatronics. https://doi.org/10.1109/TMECH.2017.2731803
35. Wang B, Liu Z (2014) Investigations on the chip formation mechanism and shear localization sensitivity of high-speed machining Ti6Al4V. Int J Adv Manuf Technol 75: 1065–1076